



5 × 25 Gbit/s WDM transmitters based on passivated graphene–silicon electro-absorption modulators

CHIARA ALESSANDRI,^{1,2,*}  INGE ASSELBERGHS,¹ STEVEN BREMS,¹ CEDRIC HUYGHEBAERT,¹ JORIS VAN CAMPENHOUT,¹ DRIES VAN THOURHOUT,²  AND MARIANNA PANTOUVAKI¹

¹IMEC, Kapeldreef 75, 3001 Leuven, Belgium

²Ghent University - IMEC, Department of Information Technology, Technologiepark-Zwijnaarde 15, 9052 Gent, Belgium

*Corresponding author: chiara.alessandri@ugent.be

Received 18 November 2019; revised 27 December 2019; accepted 30 December 2019; posted 2 January 2020 (Doc. ID 383462); published 28 January 2020

Today, one of the key challenges of graphene devices is establishing fabrication processes that can ensure performance stability and repeatability and that can eventually enable production in high volumes. In this paper, we use up-scalable fabrication processes to demonstrate three five-channel wavelength-division multiplexing (WDM) transmitters, each based on five graphene–silicon electro-absorption modulators. A passivation-first approach is used to encapsulate graphene, which results in hysteresis-free and uniform performance across the five channels of each WDM transmitter, for a total of 15 modulators. Open-eye diagrams are obtained at 25 Gb/s using 2.5 V_{pp}, thus demonstrating potential for multi-channel data transmission at 5 × 25 Gb/s on each of the three WDM transmitters. © 2020 Optical Society of America

<https://doi.org/10.1364/AO.383462>

1. INTRODUCTION

As cloud computing, big data applications, and social networking are expected to keep growing exponentially, the amount of annual global data center traffic is set to surpass 20 ZB by 2021 [1]. To meet this demand, it is estimated that data center operators will have to upgrade their networks to 1.6 Tb/s by 2022 [2]. Advanced multiplexing technologies represent an effective solution to achieve a network infrastructure that can carry more data more efficiently [3,4]. Wavelength-division multiplexing (WDM) uses different channels to carry signals at different wavelengths in a single optical fiber or waveguide simultaneously [5,6]. Next to WDM, other multiplexing solutions are space-division multiplexing (SDM) [7], based on multi-core waveguides; mode-division multiplexing (MDM) [8], with multiple guided modes; and polarization-division multiplexing (PDM), using two orthogonal polarizations together. These approaches have independent degrees of freedom and can be combined to form hybrid multiplexing systems with capacity up to Pbit/s [4]. Among these, WDM links, enabled by low loss, broadband, and low power consumption modulators, are one of the most successful technologies. WDM allows to exploit the full bandwidth of existing optical fibers, leading to a reduced construction cost. In addition, it is simple to implement, as channels can be flexibly added or removed, and the active optical equipment is shared by the different channels.

Graphene has attracted interest in recent years due to its characteristic broadband absorption, which ranges from visible to infrared. Graphene's absorption can be easily tuned through capacitive charging by applying an electric field [9], and has therefore the potential to enable active optoelectronic functionality onto passive optical waveguides, such as Si or SiN waveguides [10,11]. These properties, together with high carrier mobility, make graphene an attractive material for high-speed photonic devices [12,13], such as modulators [10,14–21] and photodetectors [22–25]. Graphene-based modulators can therefore be implemented in WDM systems to modulate the signal on different channels. Graphene integration in photonics has already been demonstrated for Mach–Zehnder modulators (MZMs) [18], microring modulators (MRMs) [10], and electro-absorption modulators (EAMs) [14–17,19,21]. Compared to graphene MZMs and MRMs, graphene EAMs offer some advantages. Graphene MZMs have a wide optical bandwidth and high extinction ratio (ER), but suffer from high insertion loss (IL), high power consumption, and large device footprint [18]. On the other hand, graphene MRMs offer lower power consumption and smaller device footprint, but fail to exploit graphene's characteristic broadband absorption due to the resonant nature of the microring [10]. In addition, MRMs suffer from tight fabrication tolerance, and therefore thermal stabilization is necessary to match the resonant wavelength of

Table 1. Waveguide Width (W_{wg}) and Device Length (L_{device}) Values Used to Fabricate the Three WDM Transmitters^a

	W_{wg} (nm)	L_{device} (μm)
WDM1	500	100
WDM2	600	100
WDM3	600	150

^aIncreasing W_{wg} and L_{device} is expected to increase the extinction ratio but also the device capacitance, and therefore to reduce the 3 dB bandwidth.

the ring to the incoming wavelength. Graphene-based EAMs offer a very wide optical bandwidth (up to 180 nm in the C-band) [17], potentially low power consumption, and low IL [15,16].

So far, the demonstration of graphene modulators has been focused on individual components, due to challenges in processing, transfer, and integration of high-quality graphene at large scale [26]. In this work, we demonstrate for the first time the integration of multiple graphene EAMs with functional silicon photonics circuits. We use three five-channel WDM transmitters, each based on five graphene-Si EAMs designed for TE-polarized light (see Table 1) and Si-based second-order microring resonators (MRRs) for wavelength multiplexing, to demonstrate uniform and hysteresis-free performance across 15 graphene EAMs. To achieve this, we employ up-scalable fabrication processes and a passivation-first approach to encapsulate the graphene layer. The three WDM transmitters are fabricated varying the waveguide width and the device length of the EAMs. For the first and second WDM transmitters, we report 5.5 dB and 5.6 dB ER across 10 nm bandwidth for five identical 100- μm -long devices with 500-nm- and 600-nm-wide waveguides, respectively. On the third transmitter, with 150- μm -long EAMs, we achieve 8.1 dB ER. Open-eye diagrams are measured at 25 Gb/s using $2.5 V_{pp}$ on each of the five channels of the three WDM transmitters, thus demonstrating potential for data transmission at 5×25 Gb/s. Compared with our preliminary results presented in Ref. [27], we show an extra channel and more detailed device characterization.

2. DESIGN AND FABRICATION

We fabricated three WDM transmitters consisting of five graphene EAMs and five second-order MRRs each, as shown in Fig. 1. Each transmitted wavelength goes through the graphene EAMs before being added to the bus waveguide of the MRRs. The channel spacing of the MRRs, acting as multiplexer (MUX), is designed to fit a grid spacing of 300 GHz (2.4 nm) and a free-spectral range (FSR) of 12 nm. The rings have a racetrack shape and are implemented with 450-nm-wide waveguides, 9 μm coupling length, 5 μm radius, and 190 nm bus-ring gap [5]. To reduce fabrication complexity and power consumption, no temperature control is used; therefore, variations in IL, resonant wavelength, and crosstalk are expected due to local non-uniformities, as shown in Ref. [5]. The first transmitter (WDM1) is made of graphene EAMs with 500-nm-wide waveguides and 100- μm -long graphene. The second (WDM2) and third (WDM3) transmitters are made of graphene EAMs with 600-nm-wide waveguides and 100- μm - and 150- μm -long

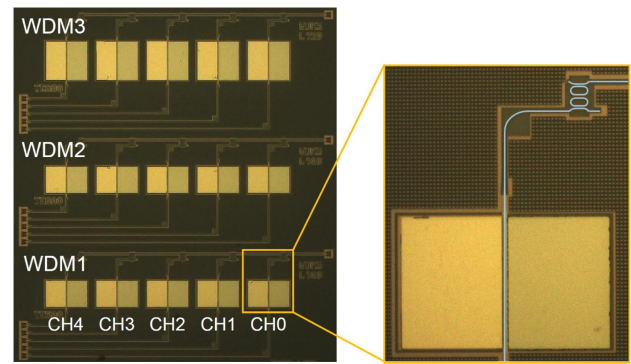


Fig. 1. Top-view microscope image showing the three WDM transmitters, each based on five graphene-Si EAMs and five second-order MRRs.

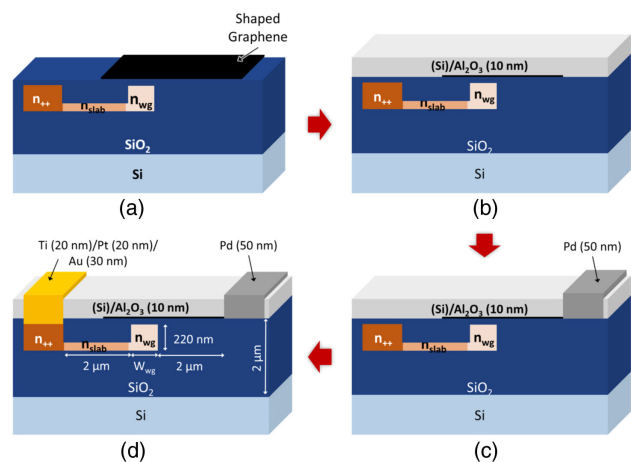


Fig. 2. Main steps of the process flow used to fabricate the graphene-Si EAMs: (a) graphene shaping, (b) Si(0.5 nm)/Al₂O₃ (10 nm) deposition, (c) graphene contact, and (d) Si contact. The passivation layer on graphene helps in obtaining uniform and hysteresis-free performance. The Si waveguide is connected to a TE-mode fiber grating coupler.

graphene, respectively. The MRRs are connected to the EAMs using tapers. Increasing the waveguide width (W_{wg}) and the device length (L_{device}) is expected to increase the ER but also the device capacitance, and therefore to reduce the 3 dB bandwidth. Each graphene EAM is based on a 220-nm-thick n-doped Si waveguide, fabricated on a SOI wafer with 2 μm buried oxide in imec's 200 mm Si photonics platform. The waveguide is partially etched on one side, leaving a 70 nm slab for electrical contact to Si. It is embedded in SiO₂ to ensure a planar surface for the subsequent graphene transfer and is designed to transmit TE-polarized light in the C-band (Fig. 2). Three separate doping levels are used to minimize the Si contact and sheet resistance, without significantly increasing the waveguide loss.

After oxide chemical-mechanical planarization (CMP), the processing is continued at coupon level in a lab environment, and graphene grown by chemical vapor deposition (CVD), commercially available from *Graphenea*, is transferred onto the substrate. Graphene-based devices show high sensitivity to environmental factors, such as ambient air, organic solvents, and

lithography resists used for fabrication [28–31]. Adsorbates on the graphene surface cause unintentional doping, while adsorbates at the graphene–SiO₂ interface affect the performance of graphene devices by introducing trap states that cause hysteretic behavior [32]. The stability of graphene devices can be improved by encapsulating graphene with a protective layer. A high- κ dielectric material is expected to screen the charged impurities at the graphene–SiO₂ interface and, if deposited at the beginning of the fabrication flow (passivation-first approach), it also protects graphene from contacting organic solvents and lithography resists during processing. Therefore, the device fabrication is carried out following a passivation-first approach. First, graphene is patterned to cover part of the Si waveguide and to define the length of the EAM [Fig. 2(a)]. After patterning, graphene is passivated with an Al₂O₃ layer [Fig. 2(b)]. Depositing the dielectric after, and not before, patterning allows to obtain full sample coverage and reduce intercalation of solvents between graphene and SiO₂ during processing. Al₂O₃ is chosen as the encapsulating material because it allows to obtain hysteresis-free electro-optical response, it preserves the p-doping characteristic of unpassivated graphene, and it is stable over time [33]. To ensure a uniform passivation layer, we first evaporate 0.5 nm of Si as seeding layer by e-gun evaporation, and then deposit 10 nm of Al₂O₃ as the capping layer by atomic layer deposition (ALD) [33]. Contacts are made to graphene (50 nm Pd) and to the doped Si (20 nm Ti/20 nm Pt/30 nm Au) using a lift-off process [Figs. 2(c) and 2(d)]. Due to the presence of the passivation layer, an etching step has to be added to remove the Al₂O₃ before depositing Pd to contact graphene. As a consequence, graphene is removed from the contact area, and a side contact between graphene and Pd is created. This contacting scheme has been shown to reduce the metal–graphene contact resistance compared to a standard top contact [34]. The contacts are placed 2 μ m away from the waveguide and therefore have no impact on transmission loss. Graphene and the Si waveguide are separated by a SiO₂ layer of 5 nm, thus forming a graphene–oxide–Si (GOS) capacitor [Fig. 2(d)]. The metal contacts are used to apply an electric field across the GOS capacitor. Due to the electric field, charges are accumulated or depleted in the graphene layer, and consequently the graphene absorption is tuned as a function of the applied voltage bias [10].

3. RESULTS AND DISCUSSION

We first performed unbiased fiber-to-fiber transmission measurements of the three WDM transmitters, each composed of five channels. The IL of each channel was calculated as the peak transmission of the channel, normalized to the transmission of a reference waveguide without graphene at the same wavelength. The extracted average and standard deviation values of IL over the five channels were 3.8 ± 1.0 dB, 2.9 ± 0.7 dB, and 4.0 ± 0.5 dB for WDM1, WDM2, and WDM3, respectively (Table 2). To determine the main source of IL, we performed transmission measurements on a WDM filter without graphene, with the same design as WDM2, located on a different die. These measurements, normalized to a reference waveguide, show that the IL due to the second-order MRRs is ~ 2 dB for CH1 and less than 1 dB for all other channels [Fig. 3(a)]. Therefore, we conclude that the loss of

Table 2. Insertion Loss (IL) and Extinction Ratio (ER) at $8 V_{pp}$ ^a

	L_{device} (μ m)	IL (dB)	ER (dB)
WDM1	100	3.8 ± 1.0	5.5 ± 0.1
WDM2	100	2.9 ± 0.7	5.6 ± 0.1
WDM3	150	4.0 ± 0.5	8.1 ± 0.7

^aThe values are averaged over five channels. WDM3 exhibits higher IL and ER due to the longer L_{device} .

the WDM transmitters is dominated by the IL of the graphene modulators.

The electro-optical response of the graphene EAMs was characterized by sweeping the wavelength from 1510 nm to 1600 nm on each channel, while applying voltage bias ranging from -4 V to 4 V. The optical power was measured at the output of the transmitters (bus waveguide). An example of this measurement performed on WDM2 is shown in Fig. 3(b) (with reduced wavelength range from 1552.5 nm to 1562.5 nm for clarity). The ER at $8 V_{pp}$ was obtained by extracting the transmission as a function of the voltage at the peak transmission wavelength of each channel [example for WDM2 in Fig. 3(c)]. The ER was consistent across all channels, with average values of 5.5 ± 0.1 dB for WDM1, 5.6 ± 0.1 dB for WDM2, and 8.1 ± 0.7 dB for WDM3 (Table 2). The higher ER in WDM3 is due to the longer device length, which ensures a longer interaction between the graphene layer and the evanescent field of the light traveling through the waveguide. The electro-optical switching in transmission occurs around 0 V, because of p-doping in graphene. The p-doping characteristic is ideal for electro-optical modulation, because it allows to operate the device at low voltage DC bias. The carrier mobility of graphene is estimated to be ~ 800 cm²/(Vs) from measurements performed on electrical test structures fabricated on the same sample. The static power consumption at -1 V is calculated to be $< 2 \times 10^{-8}$ mW, due to the < 20 pA measured leakage current.

In order to study the effect of the Al₂O₃ passivation layer on the hysteretic behavior of the EAMs, we performed double-sweep electro-optical measurements at 1560 nm wavelength on a standalone 25- μ m-long graphene EAM fabricated simultaneously on the same chip. We compared these results with the ones obtained on an unpassivated 25- μ m-long graphene EAM fabricated under the same processing conditions (Fig. 4). The unpassivated EAM shows hysteretic behavior, with a difference in transmission at 0 V between the forward and backward voltage sweeps of $\Delta T = 0.35$ dB. This behavior is not present in the passivated EAM, where ΔT is only 0.02 dB, thus showing that the Al₂O₃ passivation layer allows to obtain hysteresis-free electro-optical response, while at the same time preserving the p-doping characteristic of unpassivated graphene. The same measurement repeated on the passivated EAM after two months shows no significant degradation in the response of the device ($\Delta T = 0.16$ dB). Two parameters could be optimized to further improve stability over time. The first is the thickness of the Al₂O₃, as it has been shown to affect the performance stability of graphene field-effect devices [33]. In addition, a thick SiO₂ layer (~ 1 μ m) could be deposited on top of the Al₂O₃ to increase further the thickness of the dielectric stack. The second is the

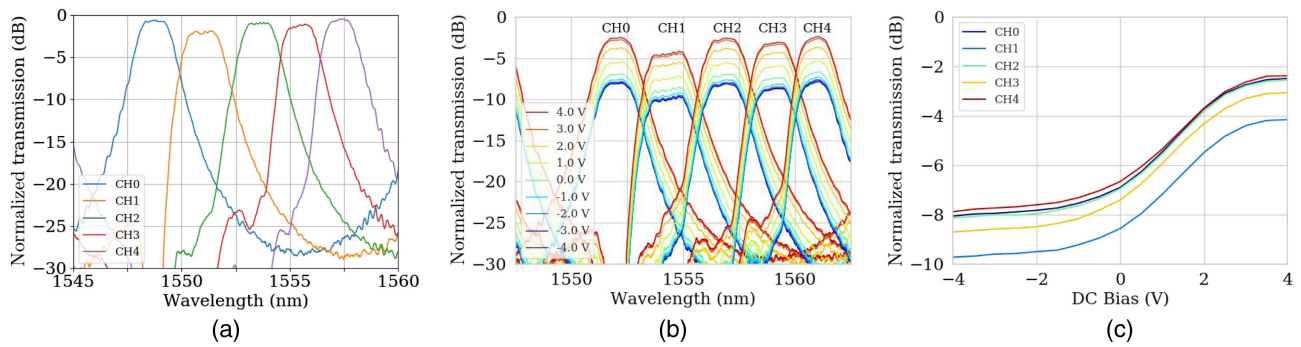


Fig. 3. (a) Transmission spectra, normalized to a reference waveguide, measured on a WDM filter without graphene, showing the insertion loss of the second-order MRRs. (b) Transmission spectra on WDM2, normalized to a reference waveguide without graphene. The voltage is varied from -4 V to 4 V on each graphene EAM, resulting in the tuning of the transmission on each channel. (c) Normalized transmission as a function of DC voltage bias, measured on WDM2. The transmission is extracted at the peak wavelength of each channel. The modulation is uniform on the five channels.

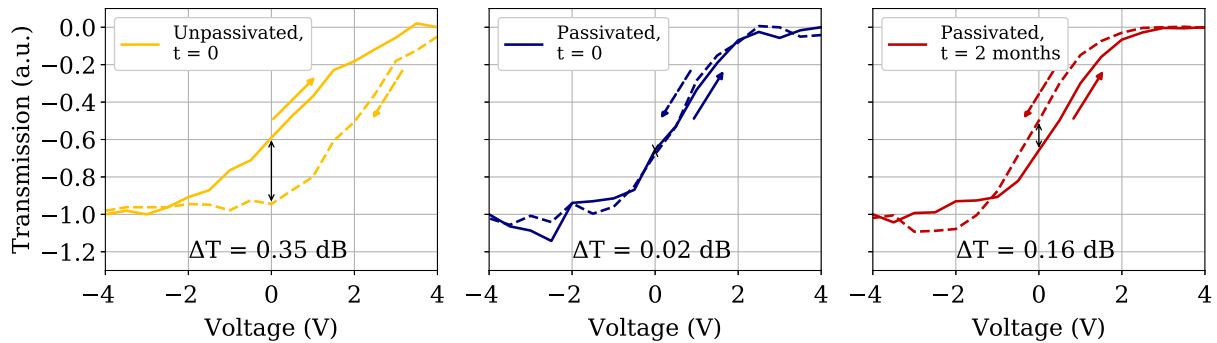


Fig. 4. Comparison of transmission curves, measured with a double-voltage sweep right after fabrication, between an unpassivated (yellow) and a passivated (blue) $25\text{-}\mu\text{m}$ -long graphene EAM. The unpassivated EAM shows hysteretic behavior, which is not present in the passivated EAM. The same measurement is repeated on the passivated EAM after two months (red), showing a small hysteresis that remains less pronounced compared to the unpassivated device.

type of seeding layer used for Al_2O_3 deposition, because it has a significant impact on the dielectric constant (κ) and morphology of ALD Al_2O_3 [35]. A higher κ would also allow to achieve a better mobility retention in graphene [36], leading to lower graphene resistance and higher ER.

The electro-optical S_{21} frequency response was measured between 100 MHz and 30 GHz on the three WDM transmitters at DC bias ranging from -2 V to 2 V with a vector network analyzer, using -8 dBm RF power. Figure 5(a) shows the S_{21} and S_{11} frequency response of WDM2 at 0 V DC bias. The trend of the 3 dB bandwidth as a function of DC bias is shown in Fig. 5(b) for WDM1. The highest 3 dB bandwidth is measured at -1 V and 0 V, where the total RC constant of the device reaches the minimum. At reverse bias, graphene's neutrality point is approached; therefore, the total resistance of graphene increases, and the 3 dB bandwidth decreases slightly. At forward bias, the GOS capacitor with n-doped Si enters the accumulation region, characterized by a drastic increase in the capacitance [Fig. 5(b)], causing a drop in the 3 dB bandwidth. Average 3 dB bandwidths of 9.5 ± 0.7 GHz, 9.3 ± 0.1 GHz, and 7.1 ± 0.3 GHz were recorded, respectively, for WDM1, WDM2, and WDM3 at 0 V DC bias. The response decreases as the waveguide width and the graphene length increase, due to the higher RC constant (Table 3).

Eye diagrams were measured at the peak wavelength of each channel using 2^7-1 pseudorandom binary sequence (PRBS) at $2.5 V_{pp}$ with a 50Ω terminated probe. The applied DC bias is different for each channel because of small variations in graphene doping, with an average value of -1.2 ± 0.2 V. Open- and symmetrical-eye diagrams were generated from 5 Gb/s to 25 Gb/s for all channels, thus allowing to transmit data up to 5×25 Gb/s on each WDM transmitter. Eye diagrams measured on the five channels of WDM2 are shown in Fig. 6. The dynamic ER and signal-to-noise ratio (SNR) of the five channels on each WDM transmitter are reported in Fig. 7 as a function of bit rate. The SNR is higher than 3.0 up to 25 Gbit/s for all the WDM transmitters. WDM3 exhibits a 45% higher ER, due to the longer graphene waveguide coverage, thus allowing to obtain open-eye diagrams up to 30 Gb/s with an SNR of 2.9 and a dynamic ER of 1.2 dB (Fig. 8). This shows that the primary limiting factor of these devices is the ER, followed by the frequency response. The dynamic energy consumption ($E_{bit} = CV^2/4$) of a single graphene EAM at -1 V is estimated to be ~ 163 fJ for WDM1, ~ 195 fJ for WDM2, and ~ 308 fJ for WDM3. These values are, to the best of our knowledge, the lowest reported for graphene-based modulators.

To further improve the performance of these devices, the thickness of the oxide between graphene and Si can be increased

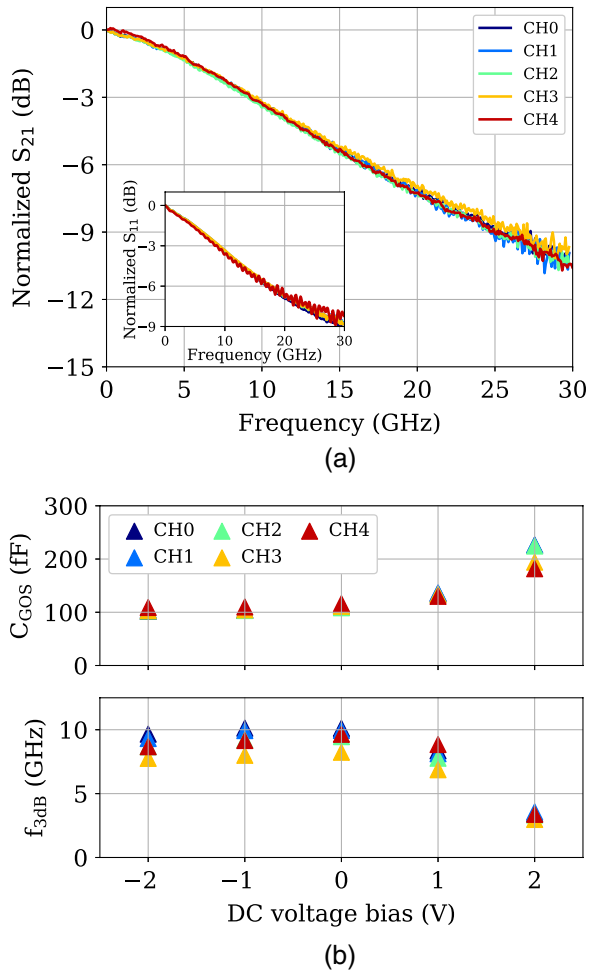


Fig. 5. (a) Electro-optical S_{21} (inset: S_{11}) frequency response measured at 0 V DC bias on WDM2. The response is uniform across the five channels. (b) GOS capacitance and 3 dB bandwidth of WDM1 as a function of DC bias. The GOS capacitance increases at forward bias, causing a drop in 3 dB bandwidth. The ideal operating region is therefore at 0 V or low reverse bias.

Table 3. Total Resistance (R_{tot}) and GOS Capacitance (C_{GOS}) Extracted from S_{11} Parameter Fitting, Simulated (from the Fitted Parameters in Columns 1 and 2) and Measured f_{3dB} at 0 V^a

	L_{device} (μm)	R_{tot} (Ω)	C_{GOS} (fF)	f_{3dB} (GHz) at 0 V	
				Simulated	Measured
WDM1	100	78 ± 5	112.6 ± 0.5	10.1 ± 0.5	9.5 ± 0.7
WDM2	100	65 ± 5	134.7 ± 0.5	9.5 ± 0.5	9.3 ± 0.1
WDM3	150	49 ± 5	206.6 ± 0.5	7.0 ± 0.5	7.1 ± 0.3

^aThe values are averaged over five channels. Due to the longer L_{device} , WDM3 exhibits higher RC constant, and therefore lower f_{3dB} .

to reduce the device capacitance and therefore the RC constant. However, this leads to a lower modulation efficiency, due to the increased DC bias and V_{pp} necessary to operate the device. Therefore, we suggest a different approach. The Si doping in the waveguide can be optimized to reduce the Si capacitance and resistance contributions in the operating region. For example,

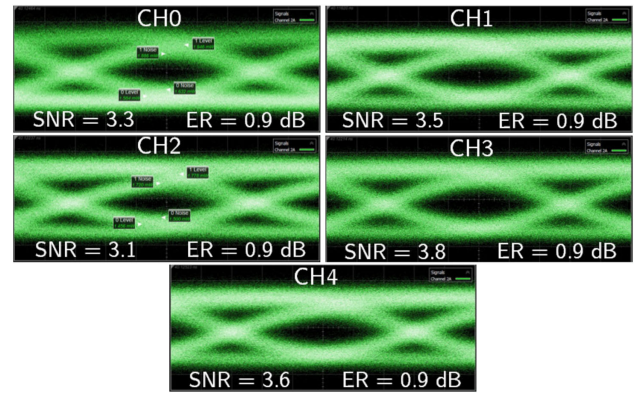


Fig. 6. Eye diagrams measured at 25 Gbit/s on WDM2 at 2.5 V_{pp} and -1.2 V DC bias. The performance is uniform across the five channels. The dynamic extinction ratio is limited by the low modal overlap with graphene when using TE-polarized light.

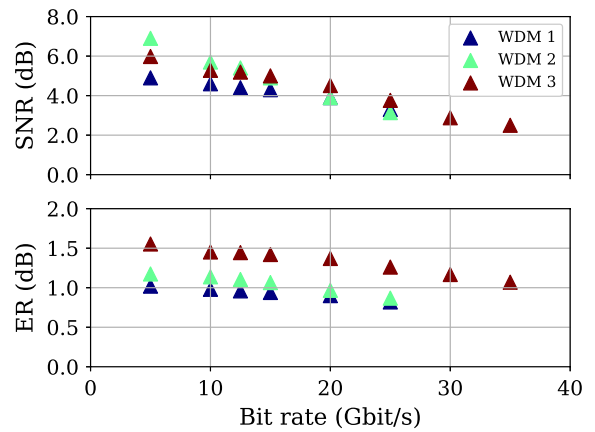


Fig. 7. SNR and dynamic ER as a function of bit rate. The SNR is higher than 3.0 up to 25 Gbit/s for all the WDM transmitters. The ER for WDM3 is higher than 1 dB up to 30 Gbit/s, due to the longer device length.

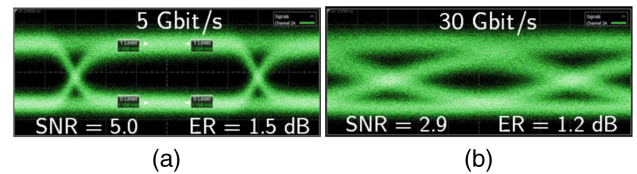


Fig. 8. Eye diagrams measured at 5 Gbit/s (a) and 30 Gbit/s (b) on CH2 of WDM3 at 2.5 V_{pp} and -1.2 V DC bias.

an improvement of $\sim 42\%$ in 3 dB frequency response can be achieved by p-doping instead of n-doping the Si waveguide without affecting the modulation efficiency, because the device can be operated in depletion mode instead of accumulation mode [37]. A two-fold improvement in ER can be attained by designing graphene-based WDM transmitters for TM- instead of TE-polarized light [15]. Furthermore, an improvement in graphene quality, and therefore in the carrier mobility of graphene, will allow to increase the ER for fixed V_{pp} , reduce graphene resistance, and reduce the IL of the graphene EAMs.

4. CONCLUSION

We demonstrated three graphene-based five-channel WDM transmitters, fabricated with an up-scalable fabrication process and with passivated graphene, to ensure uniform and hysteresis-free device performance. On each channel, the TE-polarized light was modulated using broadband graphene EAMs, for a total of 15 working devices. On the first and second transmitters, with 100- μm -long graphene EAMs, we achieved average static ERs of 5.5 ± 0.1 dB and 5.6 ± 0.1 dB, respectively. On the third transmitter, with 150- μm -long graphene EAMs, we achieved 8.1 ± 0.7 dB average static ER. Open-eye diagrams were measured in the C-band at 2.5 V_{pp} on three WDM transmitters, thus demonstrating potential for data transmission at 5×25 Gb/s.

Funding. Horizon 2020 Framework Programme (785219).

Acknowledgment. The authors acknowledge imec's industrial affiliation Optical I/O program. The authors acknowledge Ashwyn Srinivasan and Peter De Heyn for useful discussions.

Disclosures. The authors declare no conflicts of interest.

REFERENCES

1. "Cisco global cloud index: forecast and methodology, 2016–2021," in Tech. Rep. (Cisco, 2018) <https://www.cisco.com/c/en/us/solutions/collateral/service-provider/global-cloud-index-gci/white-paper-c11-738085.html>.
2. "Ethernet Alliance Roadmap," 2019, <https://www.ethernetalliance.com>.
3. P. J. Winzer, "Making spatial multiplexing a reality," *Nat. Photonics* **8**, 345–348 (2014).
4. D. Dai and J. E. Bowers, "Silicon-based on-chip multiplexing technologies and devices for peta-bit optical interconnects," *Nanophotonics* **3**, 283–311 (2014).
5. P. De Heyn, J. De Coster, P. Verheyen, G. Lepage, M. Pantouvaki, P. Absil, W. Bogaerts, J. Van Campenhout, and D. Van Thourhout, "Fabrication-tolerant four-channel wavelength-division-multiplexing filter based on collectively tuned Si microrings," *J. Lightwave Technol.* **31**, 2785–2792 (2013).
6. J. B. Driscoll, P. Doussiere, S. Islam, R. Narayan, W. Lin, H. Mahalingam, J. S. Park, Y. Lin, K. Nguyen, K. Roelofs, A. Dahal, R. Venables, L. Liao, R. Jones, D. Zhu, S. Priyadarshi, B. Parthasarathy, and Y. Akulova, "First 400G 8-channel CWDM silicon photonic integrated transmitter," in *IEEE International Conference on Group IV Photonics (GFP)* (2018).
7. K. Igarashi, D. Soma, Y. Wakayama, K. Takeshima, Y. Kawaguchi, N. Yoshikane, T. Tsuritani, I. Morita, and M. Suzuki, "Ultra-dense spatial-division-multiplexed optical fiber transmission over 6-mode 19-core fibers," *Opt. Express* **24**, 10213–10231 (2016).
8. D. Zhou, C. Sun, Y. Lai, Y. Yu, and X. Zhang, "Integrated silicon multi-functional mode-division multiplexing system," *Opt. Express* **27**, 10798–10805 (2019).
9. G. W. Hanson, "Dyadic Green's functions and guided surface waves for a surface conductivity model of graphene," *J. Appl. Phys.* **103**, 064302 (2008).
10. C. T. Phare, Y.-H. Daniel Lee, J. Cardenas, and M. Lipson, "Graphene electro-optic modulator with 30 GHz bandwidth," *Nat. Photonics* **9**, 511–514 (2015).
11. L. A. Shiramin and D. Van Thourhout, "Graphene modulators and switches integrated on silicon and silicon nitride waveguide," *IEEE J. Sel. Top. Quantum Electron.* **23**, 3600107 (2017).
12. F. Bonaccorso, Z. Sun, T. Hasan, and A. C. Ferrari, "Graphene photonics and optoelectronics," *Nat. Photonics* **4**, 611–622 (2010).
13. M. Romagnoli, V. Sorianoello, M. Midrio, F. H. L. Koppens, C. Huyghebaert, D. Neumaier, P. Galli, W. Templ, A. D'Errico, and A. C. Ferrari, "Graphene-based integrated photonics for next-generation datacom and telecom," *Nat. Rev. Mater.* **3**, 392–414 (2018).
14. C. Alessandri, I. Asselberghs, Y. Ban, S. Brems, C. Huyghebaert, J. Van Campenhout, D. Van Thourhout, and M. Pantouvaki, "Broadband 20 Gbit/s graphene-Si electro-absorption modulator," in *European Conference on Optical Communication (ECOC)* (2018).
15. Y. Hu, M. Pantouvaki, J. Van Campenhout, S. Brems, I. Asselberghs, C. Huyghebaert, P. Absil, and D. Van Thourhout, "Broadband 10 Gb/s operation of graphene electro-absorption modulator on silicon," *Laser Photon. Rev.* **10**, 307–316 (2016).
16. M. Liu, X. Yin, E. Ulin-avila, B. Geng, T. Zentgraf, L. Ju, F. Wang, and X. Zhang, "A graphene-based broadband optical modulator," *Nature* **474**, 64–67 (2011).
17. M. Mohsin, D. Schall, M. Otto, A. Nocolak, D. Neumaier, and H. Kurz, "Graphene based low insertion loss electro-absorption modulator on SOI waveguide," *Opt. Express* **22**, 15292–15297 (2014).
18. V. Sorianoello, M. Midrio, G. Contestabile, I. Asselberghs, J. Van Campenhout, C. Huyghebaert, I. Goykhman, A. K. Ott, A. C. Ferrari, and M. Romagnoli, "Graphene-silicon phase modulators with gigahertz bandwidth," *Nat. Photonics* **12**, 40–44 (2018).
19. V. Sorianoello, G. Contestabile, M. Midrio, M. Pantouvaki, I. Asselberghs, J. Van Campenhout, C. Huyghebaerts, A. D'Errico, P. Galli, and M. Romagnoli, "Chirp management in silicon-graphene electro absorption modulators," *Opt. Express* **25**, 19371–19381 (2017).
20. H. Dalir, Y. Xia, Y. Wang, and X. Zhang, "Athermal broadband graphene optical modulator with 35 GHz speed," *ACS Photon.* **3**, 1564–1568 (2016).
21. M. A. Giambra, V. Sorianoello, V. Miseikis, S. Marconi, A. Montanaro, P. Galli, S. Pezzini, C. Coletti, and M. Romagnoli, "High-speed double layer graphene electro-absorption modulator on SOI waveguide," *Opt. Express* **27**, 20145–20155 (2019).
22. A. Pospischil, M. Humer, M. M. Furchi, D. Bachmann, R. Guider, T. Fromherz, and T. Mueller, "CMOS-compatible graphene photodetector covering all optical communication bands," *Nat. Photonics* **7**, 892–896 (2013).
23. X. Gan, R.-J. Shiue, Y. Gao, I. Meric, T. F. Heinz, K. Shepard, J. Hone, S. Assefa, and D. Englund, "Chip-integrated ultrafast graphene photodetector with high responsivity," *Nat. Photonics* **7**, 883–887 (2013).
24. I. Goykhman, U. Sassi, B. Desiatov, N. Mazurski, S. Milana, D. De Fazio, A. Eiden, J. Khurgin, J. Shappir, U. Levy, and A. C. Ferrari, "On-chip integrated, silicon-graphene plasmonic Schottky photodetector with high responsivity and avalanche photogain," *Nano Lett.* **16**, 3005–3013 (2016).
25. D. Schall, C. Porschatis, M. Otto, and D. Neumaier, "Graphene photodetectors with a bandwidth >76 GHz fabricated in a 6" wafer process line," *J. Phys. D* **50**, 124004 (2017).
26. S. Brems, K. Verguts, N. Vrancken, B. Vermeulen, C. Porret, L. Peters, C. H. Wu, C. Huyghebaert, K. Schouteden, C. Van Haesendonck, and S. De Gendt, "Graphene synthesis and transfer improvements for applications in the semiconductor industry," *ECS Trans.* **77**, 3–13 (2017).
27. C. Alessandri, I. Asselberghs, P. D. Heyn, S. Brems, J. Van Campenhout, and D. Van Thourhout, "4-channel C-Band WDM transmitter based on 10 GHz graphene-silicon electro-absorption modulators," in *Optical Fiber Communication Conference* (2019).
28. S. Adam, E. H. Hwang, V. M. Galitski, and S. Das Sarma, "A self-consistent theory for graphene transport," *Proc. Natl. Acad. Sci. USA* **104**, 18392–18397 (2007).
29. H. Wang, Y. Wu, C. Cong, J. Shang, and T. Yu, "Hysteresis of electronic transport in graphene transistors," *ACS Nano* **4**, 7221–7228 (2010).
30. P. Joshi, H. E. Romero, A. T. Neal, V. K. Toutam, and S. A. Tadiadapa, "Intrinsic doping and gate hysteresis in graphene field effect devices fabricated on SiO₂ substrates," *J. Phys. Condens. Matter* **22**, 334214 (2010).

31. Y. G. Lee, C. G. Kang, U. J. Jung, J. J. Kim, H. J. Hwang, H. J. Chung, S. Seo, R. Choi, and B. H. Lee, "Fast transient charging at the graphene/SiO₂ interface causing hysteretic device characteristics," *Appl. Phys. Lett.* **98**, 183508 (2011).
32. H. Xu, Y. Chen, J. Zhang, and H. Zhang, "Investigating the mechanism of hysteresis effect in graphene electrical field device fabricated on SiO₂ substrates using Raman spectroscopy," *Small* **8**, 2833–2840 (2012).
33. A. A. Sagade, D. Neumaier, D. Schall, M. Otto, A. Pesquera, A. Centeno, A. Z. Elorza, and H. Kurz, "Highly air stable passivation of graphene based field effect devices," *Nanoscale* **7**, 3558–3564 (2015).
34. D. W. Yue, C. H. Ra, X. C. Liu, D. Y. Lee, and W. J. Yoo, "Edge contacts of graphene formed by using a controlled plasma treatment," *Nanoscale* **7**, 825–831 (2015).
35. B. Fallahzad, K. Lee, G. Lian, S. Kim, C. M. Corbet, D. A. Ferrer, L. Colombo, and E. Tutuc, "Scaling of Al₂O₃ dielectric for graphene field-effect transistors," *Appl. Phys. Lett.* **100**, 093112 (2012).
36. S. A. Imam, A. Guermoune, M. Siaj, and T. Szkopek, "Oxide and nitride encapsulation of large-area graphene field effect devices," *Thin Solid Films* **520**, 7041–7043 (2012).
37. C. Alessandri, I. Asselberghs, S. Brems, C. Huyghebaert, J. Van Campenhout, D. Van Thourhout, and M. Pantouvaki, "High speed single-layer graphene-Si electro-absorption modulator," in *Conference on Lasers and Electro-Optics Pacific Rim (CLEO-PR)*, OSA Technical Digest (2018), paper Th4G3.